MATERIALS CHEMISTRY
FRONTIERS

RESEARCH ARTICLE

View Article Online
View Journal | View Issue

Cite this: *Mater. Chem. Front.*, 2018, **2**, 1811

A novel lithium-ion hybrid capacitor based on an aerogel-like MXene wrapped Fe_2O_3 nanosphere anode and a 3D nitrogen sulphur dual-doped porous carbon cathode†

Xiao Tang,[a] Hao Liu,[a] Xin Guo,[a] Shijian Wang,[b] Wenjian Wu,[b] Anjon Kumar Mondal,[a] Chengyin Wang[c] and Guoxiu Wang*[a]

Received 14th May 2018,
Accepted 16th July 2018

DOI: 10.1039/c8qm00232k

rsc.li/frontiers-materials

Lithium-ion capacitors (LICs) have emerged as promising energy storage devices with both high energy density and high power density. However, due to the mismatch of charge-storage capacity and electrode kinetics between battery-type anodes and capacitor-type cathodes, the application of lithium-ion capacitors has been limited. In this work, interconnected aerogel-like MXene wrapped Fe_2O_3 nanospheres have been prepared and investigated as battery-type anode materials for lithium-ion capacitors. In this rationally designed hybrid electrode, the $Ti_3C_2T_x$ MXene matrix is capable of providing fast transport of electrons and suppressing the volume change of Fe_2O_3. Simultaneously, Fe_2O_3 hollow nanospheres offer large specific capacity and prevent restacking of the MXene layers, synergizing to boost the electrochemical performances of such hybrid electrodes. Meanwhile, the three-dimensional (3-D) nitrogen and sulphur dual-doped porous carbon (NS-DPC) derived from biomass has also been fabricated as a capacitor-type cathode material for lithium-ion capacitors. Consequently, the lithium-ion capacitors can demonstrate a high energy density of 216 W h kg^{-1} at a power density of 400 W kg^{-1} and a high power density of 20 kW kg^{-1} at an energy density of 96.5 W h kg^{-1}. This work elucidates that both high energy density and power density can be achieved in hybrid lithium-ion capacitors.

Introduction

With the soaring demand for portable electronic devices, hybrid electric vehicles, and large-scale electricity grid storage, future energy-storage devices are required to possess features of high energy density, high power density and superior cycling stability.[1] Lithium-ion batteries (LIBs) can provide a high energy density of ~150 W h kg^{-1}.[2] Nevertheless, intrinsically slow solid-state diffusion and volumetric strain lead to low power density. In contrast, supercapacitors (SCs) are able to deliver a high power density of 2–5 kW kg^{-1} and an excellent cycling performance. However, as charges are only stored on the surface of the active material, SCs usually suffer from low energy density (3–6 W h kg^{-1}). Hence, the development of new energy-storage devices with features of both LIBs and SCs is highly desirable.[3,4]

Recently, lithium-ion capacitors (LICs) have been proposed to bridge the gap between LIBs and SCs, and to deliver higher power density than LIBs and higher energy density than SCs. LICs have previously been constructed by an LIB-type anode with large capacity, an SC-type cathode with superior rate capability and nonaqueous Li-salt-containing electrolyte that can provide a wide working voltage window.[2–4] So far, in order to optimize the electrochemical performance of LICs, various electrode materials have been developed.[5] Many carbonaceous materials, including active carbon,[3,6] graphene,[7–9] dual-doped carbon nanofibers[10] and metal–organic-framework derived carbon, have been reported as cathodes for LICs. In addition, for LIB-type anodes, insertion-type materials (TiO_2,[7,11–13] Nb_2O_5,[14] FeOOH,[15] $Li_4Ti_5O_{12}$,[16–18] and graphite,[19–22] *etc.*), conversion-type materials (such as MnO, F-doped Fe_2O_3[23] and Fe_3O_4,[8] *etc.*) and alloy-type materials (including Sn-encapsulated nitrogen-rich CNT,[24] Si/Cu,[25] *etc.*) have been utilized to realize high-performance LICs with both high energy density and power density.

Fe_2O_3 has attracted tremendous attention due to its high specific capacity, low voltage plateau, low-cost and eco-friendliness.[26–29] Nevertheless, the poor ionic/electronic conductivities cause sluggish transport of lithium ions and electrons, therefore leading to inferior

[a] *Centre for Clean Energy Technology, Faculty of Science, University of Technology Sydney, Sydney, NSW 2007, Australia. E-mail: guoxiu.wang@uts.edu.au*
[b] *Department of Materials Science and Engineering, Dongguan University of Technology, Dongguan, China*
[c] *College of Chemistry and Chemical Engineering, Yangzhou University, Yangzhou, China*

† Electronic supplementary information (ESI) available: Additional characterization and electrochemical tests. See DOI: 10.1039/c8qm00232k

rate performance. In addition, huge volume expansion during charge and discharge processes can result in pulverization of the electrode and short cycle life. Particularly, the lack of a continuous conductive matrix and electron transport pathway usually leads to low utilization of active materials.[28]

Significant efforts have been devoted to preparing nanosized Fe_2O_3 hollow spheres as electrode materials, which is an effective method to shorten the diffusion pathway during charge/discharge processes.[30] However, the low electrical conductivity and inferior cycling stability are still the crucial concerns for Fe_2O_3-based materials as high-performance electrodes for lithium-ion capacitors.[31] Therefore, it is highly desirable to fabricate Fe_2O_3 composite electrodes with high capacity, good rate performance and long cycling stability.

Several conductive matrices including graphene,[28,32] mesoporous carbon[33–35] and polymers[30,36] were adopted to combine with Fe_2O_3. $Ti_3C_2T_x$ MXene (T_x represents the surface functional groups, such as –OH, –F, or =O) with an aerogel-like architecture is emerging as a promising conductive matrix to support Fe_2O_3. The aerogel-like MXene wrapped Fe_2O_3 nanosphere (noted as $Ti_3C_2T_x$@Fe_2O_3) nanocomposites have several advantages: (i) $Ti_3C_2T_x$ MXene, which exhibits excellent conductivity, not only acts as an interconnected network to load Fe_2O_3 and provide an efficient electron transport pathway, but also imparts some charge storage capacity for the whole composite, since $Ti_3C_2T_x$ MXene itself is one of the pseudocapacitive anodes for LICs.[37–40] (ii) Fe_2O_3 can be adsorbed onto the aerogel-like $Ti_3C_2T_x$ MXene with a porous structure and large surface area *via* ion-exchange and electrostatic interactions, therefore suppressing the detachment of Fe_2O_3 from the matrix during electrochemical reactions. (iii) MXene layers are capable of confining the volume change of Fe_2O_3 during charge/discharge processes, avoiding pulverization. Meanwhile, Fe_2O_3 anchored on the surface of MXene plays a role as a spacer, which can prevent restacking of the MXene layers induced by van der Waals interaction and hydrogen bonds. Thus, the "pillar effect" of Fe_2O_3 between $Ti_3C_2T_x$ MXene layers and synergistic effects between the Fe_2O_3 and the $Ti_3C_2T_x$ MXene matrix together endow the nanocomposite with excellent electrochemical performances as a promising electrode material for lithium-ion capacitors.

Herein, we report the successful fabrication of an interconnected aerogel-like architecture by distributing porous Fe_2O_3 hollow nanospheres onto the aerogel-like $Ti_3C_2T_x$ MXene *via* a surfactant. The $Ti_3C_2T_x$@Fe_2O_3 hybrid electrodes achieve a large specific capacity and an excellent rate performance. We also explored the capacity contribution from diffusion-controlled and pseudocapacitive currents in the hybrid electrode. Furthermore, three-dimensional (3-D) nitrogen and sulphur dual-doped porous carbon (NS-DPC) has also been prepared as a capacitor-type cathode material for lithium-ion capacitors. Consequently, a 4 V lithium-ion capacitor based on the aerogel-like MXene wrapped Fe_2O_3 nanosphere anode and the 3-D NS-DPC cathode was assembled, exhibiting a high energy density of 216 W h kg^{-1} at a power density of 400 W kg^{-1} and a high power density of 20 kW kg^{-1} at an energy density of 96.5 W h kg^{-1}.

Experimental section

Synthesis of Fe_2O_3 hollow nanospheres

The Fe_2O_3 hollow nanospheres were prepared according to the previously reported method.[41] In a typical procedure, 0.42 g of $Na_4Fe(CN)_6$, 0.04 g of hexadecyltrimethyl ammonium bromide (CTAB), 0.18 g of $(NH_4)_2S_2O_8$ and 0.18 g of NaH_2PO_4 were dissolved in 100 mL distilled water. After 30 minutes of magnetic stirring at room temperature, a yellow transparent solution was obtained and then transferred into a Teflon-lined autoclave, followed by a hydrothermal treatment at 180 °C for 8 hours. After cooling down to room temperature, the products were rinsed several times with distilled water and dried at 80 °C overnight. Finally, the pristine Fe_2O_3 hollow nanospheres can be obtained by annealing the as-prepared products in an Ar atmosphere at 450 °C for 2 hours.

Synthesis of aerogel-like $Ti_3C_2T_x$ MXene

Ti_3AlC_2 with a particle size of <38 μm was synthesized according to a previous report.[42] Then, 3 g of Ti_3AlC_2 powder was etched in a mixture of lithium fluoride (LiF, 3 g, Alfa Aesar) and 9 M hydrochloric acid (HCl, 30 mL, Fisher Scientific) at ~35 °C for 24 hours to extract the Al atoms and obtain a multilayered $Ti_3C_2T_x$ suspension. The obtained suspension was rinsed several times with distilled water and centrifuged (3500 rpm) until the pH of the supernatant was >5. To prepare aerogel-like $Ti_3C_2T_x$, distilled water was added into the as-prepared suspension with a weight ratio of $Ti_3C_2T_x$ to water of 1 : 100. Then, the diluted suspension was sonicated under an Ar atmosphere for 1 hour and frozen by liquid nitrogen, followed by a freeze-dry process to obtain aerogel-like $Ti_3C_2T_x$.

Synthesis of an aerogel-like MXene wrapped Fe_2O_3 nanosphere nanocomposite

0.7 g Fe_2O_3 and 0.05 g cetyltrimethylammonium bromide (CTAB) were mixed in 20 mL distilled water. After 30 minutes of sonication, a red solution denoted as solution A can be obtained. Then, 0.3 g aerogel-like $Ti_3C_2T_x$ was distributed in 10 mL distilled water to prepare solution B. Solution A (CTAB-grafted Fe_2O_3) was added dropwise into solution B under stirring. The mixture was sonicated for 30 minutes and frozen by liquid nitrogen, followed by a freeze-dry process to obtain an aerogel-like $Ti_3C_2T_x$@Fe_2O_3 nanocomposite. The mass loading ratio of Fe_2O_3 in the composites was around 70 wt%.

Synthesis of 3-D nitrogen and sulphur dual-doped porous carbon (NS-DPC)

As illustrated in Scheme S1 (ESI†), *Sterculia lychnophora* were first soaked in warm distilled water until a spongy precursor was obtained. Then, the precursor was frozen by liquid nitrogen, followed by a freeze-dry process to obtain cryo-dried *Sterculia lychnophora*, which were further ground to a powder by using a household blender. The obtained powders (~4 g) were mixed in a mortar with $KHCO_3$ in a mass ratio of 1 : 4. The mixed powders were calcined at 800 °C for 5 hours under an argon atmosphere in a tube furnace. After carbonization,

the as-prepared products were washed several times with 1 M HCl and distilled water and then dried at 80 °C overnight under vacuum to obtain 3-D nitrogen and sulphur dual-doped porous carbon materials (NS-DPC).

Characterization

The XRD patterns of the as-prepared samples were collected by using a Bruker D8 discover XRD with Cu Kα radiation (40 kV and 40 mA) and a step scan of 0.02°, 5°–80° 2θ ranges and a step time of 0.5 s. Raman spectra were measured using a Renishaw inVia Raman spectrometer system (Gloucestershire, UK) equipped with a Leica DML Bmicroscope (Wetzlar, Germany) and a 17 mW at 633 nm Renishaw helium neon laser source. The specific surface area was determined by the gas sorption technique using a Micromeritics 3Flex analyser based on the Brunauer–Emmett–Teller (BET) method. X-ray photoelectron spectroscopy (XPS) measurements were performed on a Kratos XSAM-800 spectrometer with an Mg Kα radiation source. The morphology of the samples was observed using a scanning electron microscope (SEM) (Zeiss Supra 55VP, Germany) and a transmission electron microscope (TEM) (JEOL JEM-2011, Japan) with an accelerating voltage of 200 kV.

Electrochemical tests

The $Ti_3C_2T_x$@Fe_2O_3 hybrid anodes/porous carbon cathodes were prepared by mixing 80% active materials, 10% carbon black, and 10% PVDF used as a binder to form a slurry, which was then coated on copper/aluminium foil, followed by drying at 60 °C in a vacuum oven overnight. For anode tests, half-cells were assembled using $Ti_3C_2T_x$@Fe_2O_3 hybrid anodes and Li foils in 2032 type stainless steel coin cells, where the electrolyte was 1.0 M $LiPF_6$ dissolved in ethylene carbonate and diethyl carbonate (EC/DEC, v/v = 1 : 1). For cathode tests, half-cells were assembled using a porous carbon cathode and Li foils in 2032 type stainless steel coin cells while other conditions remain the same. Galvanostatic charge–discharge measurements were performed on a LAND battery test system. CV and EIS measurements were conducted on an electrochemical workstation (CHI 660D). All the tests were carried out at room temperature. The mass loadings of the $Ti_3C_2T_x$@Fe_2O_3 hybrid and porous carbon electrodes were about 1.2 and 2 mg cm^{-2}, respectively. Prelithiated $Ti_3C_2T_x$@Fe_2O_3 electrodes were selected for the anodes and porous carbon electrodes were applied as cathodes with a cathode/anode mass ratio of ~5 : 1. During the prelithiation process, the anode was directly put in contact with the Li foil in the same electrolyte for 12 hours. Then, the anode was washed with DEC and shifted to the assembly of coin cell-type hybrid capacitors.

Results and discussion

As illustrated in Scheme 1a, $Ti_3C_2T_x$ MXene was prepared *via* selectively etching Al atoms, during which functional groups (such as –OH, –F, or =O) were attached on the surface of the MXene.[38,39] Subsequently, a freeze-drying process was adopted to swell the MXene layers to form an aerogel-like MXene matrix. Meanwhile, the BET surface area was increased from 126 m^2 g^{-1} (etched-$Ti_3C_2T_x$) to 367 m^2 g^{-1} (aerogel-like $Ti_3C_2T_x$) (shown in Fig. S1, ESI†). However, due to the van der Waals interaction and hydrogen bonding, MXene layers tend to restack again and then lead to reduced surface area.[40,43,44] Hence, Fe_2O_3 hollow nanospheres consisting of numerous subcomponent nanoparticles with a size of 5–10 nm (as shown in Fig. S2, ESI†) were introduced as "pillars" to prevent the restacking of the MXene layers. As illustrated in Scheme 1b, hollow nanospheres tend to collapse, which is caused by volume change during charge/discharge processes without the MXene protection. In contrast, when anchored on the MXene matrix, the volume change of the Fe_2O_3 hollow nanospheres can be confined by the MXene matrix and the hollow structure of the Fe_2O_3 nanospheres can buffer the volume change. Thus, the aerogel-like $Ti_3C_2T_x$@Fe_2O_3 nanocomposite is expected to possess satisfactory cycling performance owing to the "pillar effect".

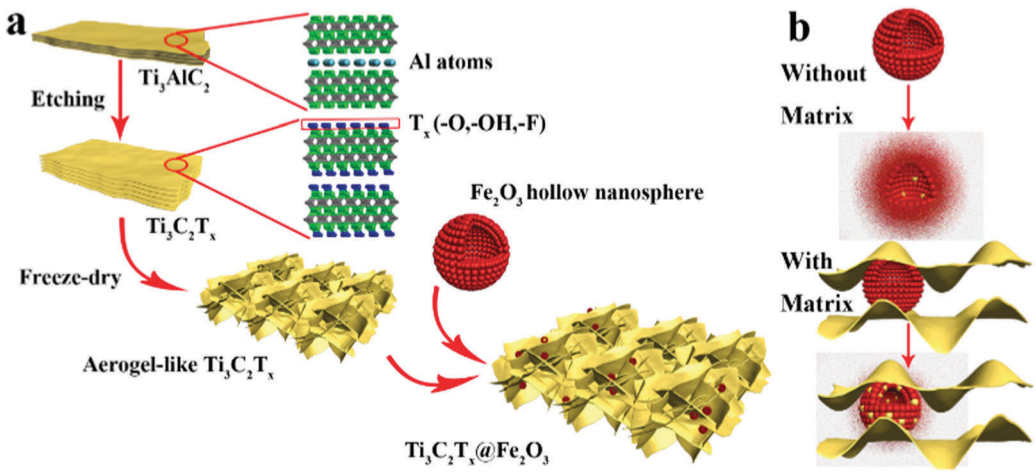

Scheme 1 (a) Schematic illustration of the synthesis procedure for the $Ti_3C_2T_x$@Fe_2O_3 nanocomposite. (b) The mechanism of the MXene matrix protection in the $Ti_3C_2T_x$@Fe_2O_3 nanocomposite.

X-ray diffraction (XRD) analysis was performed to investigate the phase of the as-prepared samples. Fig. 1a shows the XRD patterns of the obtained Fe_2O_3, $Ti_3C_2T_x$ and $Ti_3C_2T_x$@Fe_2O_3 nanocomposites. In the XRD pattern of the $Ti_3C_2T_x$@Fe_2O_3, the peak at around 7° can be ascribed to the (0001) plane of $Ti_3C_2T_x$ MXene, suggesting the existence of multilayer sheets in the as-prepared $Ti_3C_2T_x$ MXene,[45–47] whereas other diffraction peaks of the $Ti_3C_2T_x$@Fe_2O_3 are fitted well with hematite (JCPDS card no. 33-0664).[27] It is worth noticing that no impurity (such as titanium oxide, *etc.*) is observed, indicating the successful synthesis of the $Ti_3C_2T_x$@Fe_2O_3 composite without oxidation of $Ti_3C_2T_x$. To further confirm the phase and composition of the $Ti_3C_2T_x$@Fe_2O_3 composite, Raman spectra were measured (in Fig. 1b). Since the hematite belongs to the D_{3d}^6 crystal space group, two peaks located at 218 and 282 cm^{-1} can be indexed to A_{1g} and E_g bands, respectively.[48] In addition to two peaks from Fe_2O_3, the other two peaks at 201 and 380 cm^{-1} correspond to specific $Ti_3C_2T_x$ MXene bands.[49] No peak shift is observed after combination of Fe_2O_3 and $Ti_3C_2T_x$, indicating the good phase stability of the composite. X-ray photoelectron spectrum (XPS) measurements were also conducted to study the chemical composition and oxidation state of the $Ti_3C_2T_x$@Fe_2O_3 composite. The survey-scan XPS spectrum in Fig. S3 (ESI†) clearly shows the Fe, Ti, C and O signals in the composite sample. As shown in Fig. 1c, the Fe 2p core level XPS spectrum of the $Ti_3C_2T_x$@Fe_2O_3 composite shows two main peaks at

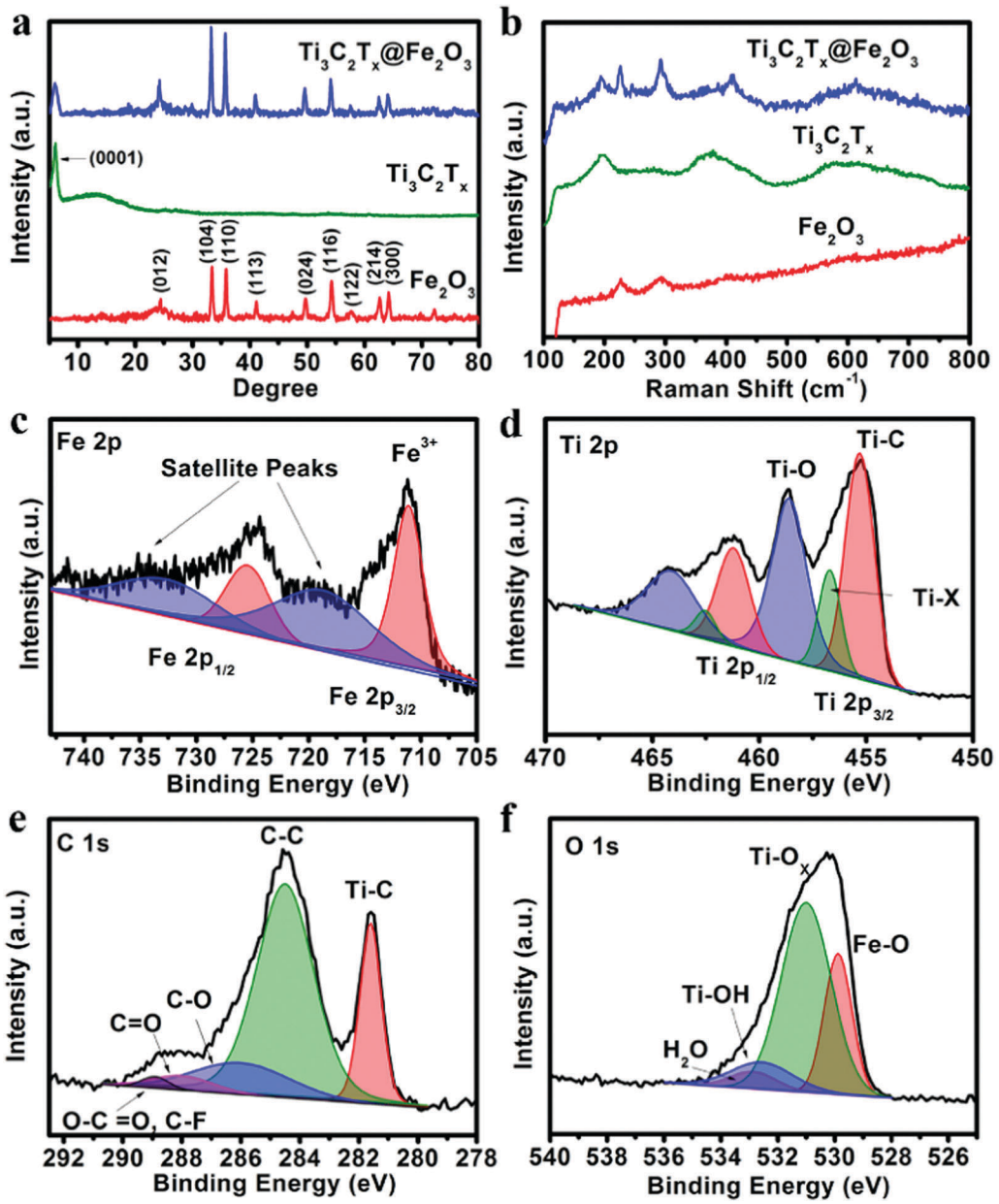

Fig. 1 (a) XRD patterns and (b) Raman spectra of the Fe_2O_3, $Ti_3C_2T_x$ and $Ti_3C_2T_x$@Fe_2O_3 samples. (c) Fe 2p, (d) Ti 2p, (e) C 1s, and (f) O 1s XPS spectra of the $Ti_3C_2T_x$@ Fe_2O_3 nanocomposite.

711.4 and 725 eV and two satellite peaks at 719.0 and 732.2 eV, which can be assigned to the characteristic peak of Fe^{3+} in hematite.[28,50,51] Fig. 1d shows the high-resolution XPS spectrum of the Ti 2p core level. Two doublets at 455.2 and 458.5 eV correspond to Ti $2p_{3/2}$, while another two doublets at 461.2 and 464.1 eV correspond to Ti $2p_{1/2}$. For the Ti $2p_{3/2}$, there are three deconvoluted peaks at 455.2, 456.9 and 458.5 eV, corresponding to Ti–C bonds, Ti–X bonds and Ti–O bonds on the surface, respectively.[52] Similarly, for Ti $2p_{1/2}$, three deconvoluted peaks at 461.2, 462.6 and 464.1 eV are observed. Fig. 1e shows the C 1s spectrum, which can be deconvoluted into five peaks at 281.7, 284.8, 286.3, 288.3 and 289.2 eV. The peak at 281.7 eV can be assigned to the C–Ti bond. The peak at 284.8 eV and 286.3 eV can be assigned to C–C and C–O, respectively. The other two peaks situated at 288.3 and 289.2 eV, can be indexed to the signals of C═O and O–C═O/C–F, respectively.[53] Fig. 1f shows the O 1s spectrum, which can be deconvoluted into four peaks centred at 529.8, 531.2, 532.8 and 533.1 eV, corresponding to Fe–O, Ti–O_x, Ti–OH and H–O (hydroxide), respectively.[54] Thus, the results of XRD, Raman, and XPS spectra convincingly confirm the successful synthesis of $Ti_3C_2T_x$@Fe_2O_3 nanocomposites.

The morphologies and crystal structures of $Ti_3C_2T_x$@Fe_2O_3 were further characterized by SEM and TEM. As shown in Fig. 2a, Fig. S2 and S4 (ESI†), the $Ti_3C_2T_x$@Fe_2O_3 composite inherits the morphological characteristics of aerogel-like MXene and porous Fe_2O_3 hollow nanospheres with a large amount of nanospheres well-distributed in the pores of the aerogel-like MXene, therefore facilitating electron transportation through the interconnected highly-conductive MXene networks. Furthermore, Fig. 2b shows the high-resolution SEM image of the $Ti_3C_2T_x$@Fe_2O_3 composite. The Fe_2O_3 nanospheres with an average size of 200 nm are observed to be tightly wrapped by few-layer MXene sheets, which is also confirmed by the TEM image (as shown in Fig. 2c). Fig. S5 (ESI†) demonstrates the EDS spectrum of the as-prepared $Ti_3C_2T_x$@Fe_2O_3 composite, confirming the co-existence of Fe, Ti, C, O and F elements. The HRTEM image (Fig. 2d) of the selected area (marked by red circle) in Fig. 2c reveals an interlayer space of about 1 nm, suggesting that the MXene sheets are multilayer. Fig. 2e shows an HRTEM image taken from the selected region (marked by red box) of the $Ti_3C_2T_x$@Fe_2O_3 composite in Fig. 2c. An interplanar lattice fringe of 0.27 nm is detected, which can be attributed to the (104) plane of hematite, again confirming the successful loading of Fe_2O_3 nanospheres. Moreover, scanning transmission electron microscopy (STEM) analysis is able to provide more information on the detailed morphology and elemental distribution of the as-prepared $Ti_3C_2T_x$@Fe_2O_3 composite. As depicted in Fig. 2f–k, the distributions of the Fe, Ti, O, C and F elements are highly consistent with the contour of the $Ti_3C_2T_x$@Fe_2O_3 composite. Notably, the contour of the Ti element map is observed to cover the contour of the Fe element map, illustrating the evenly distributed Fe_2O_3 nanospheres on the MXene matrix.

Owning to the synergistic effect of the highly conductive MXene matrix and porous Fe_2O_3 hollow nanospheres, the $Ti_3C_2T_x$@Fe_2O_3 anode is expected to exhibit improved rate and cycling performance. As shown in Fig. 3a, a high initial

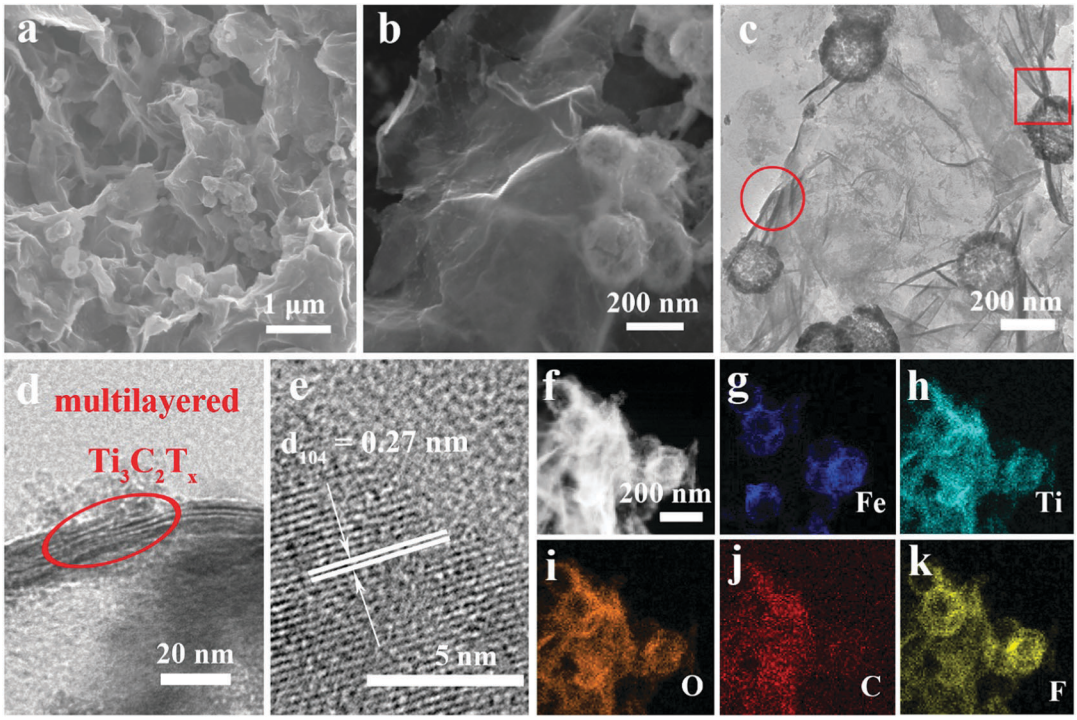

Fig. 2 (a and b) SEM images of the aerogel-like $Ti_3C_2T_x$@Fe_2O_3 composite. (c) TEM image of the aerogel-like $Ti_3C_2T_x$@Fe_2O_3 composite. (d and e) HRTEM images of the $Ti_3C_2T_x$@Fe_2O_3 composite. The circle and box in panel (c) correspond to the HRTEM images for the selected area of panel (d) and (e), respectively. (f–k) Elemental mapping of the $Ti_3C_2T_x$@Fe_2O_3 composite.

discharge capacity of 1645 mA h g^{-1} and a charge capacity of 1201 mA h g^{-1} are achieved at a current density of 0.1 A g^{-1}, corresponding to an initial coulombic efficiency of 73%, which can be ascribed to the formation of a solid electrolyte interphase (SEI) layer. This irreversible capacity loss only occurred in the first few cycles and the coulombic efficiency increased to ~100% in subsequent cycles. Fig. 3b and Fig. S6 (ESI†) presents the rate performance of the $Ti_3C_2T_x$@Fe_2O_3 anode at different current densities from 0.1 A g^{-1} to 5 A g^{-1}. It can deliver 1180, 1031, 910, 745 and 625 mA h g^{-1} at the current densities increasing from 0.1 to 2 A g^{-1}, respectively. Even at a current density of 5 A g^{-1}, a specific capacity of 493 mA h g^{-1} is retained, demonstrating an enhanced rate performance of the $Ti_3C_2T_x$@Fe_2O_3 anode. This value is markedly higher than those of other reported anode materials, such as 3D-graphene@Fe_2O_3,[28] MXene@SnO_2[37] and Fe_2O_3@polyaniline.[30] We also tested the $Ti_3C_2T_x$@Fe_2O_3 composite synthesized with different mass ratios ($Ti_3C_2T_x$: Fe_2O_3 = 1 : 1). As shown in Fig. S7 (ESI†), although the rate capability was improved, the capacity of the composite electrode decreased to ~886 mA h g^{-1} at a current density of 0.1 A g^{-1}. Meanwhile, as shown in Fig. 3b, although the initial discharge capacity of the pristine Fe_2O_3 anode is high (~1960 mA h g^{-1}), it exhibits a poor rate performance (only ~110 mA h g^{-1} at the current density of 5 A g^{-1} with capacity retention of ~5%). Thus, the combination of Fe_2O_3 and an MXene matrix has a great advantage compared with the pristine Fe_2O_3 and MXene. The increase of electroconductivity from the pristine Fe_2O_3 to $Ti_3C_2T_x$@Fe_2O_3 was further confirmed by Electrochemical

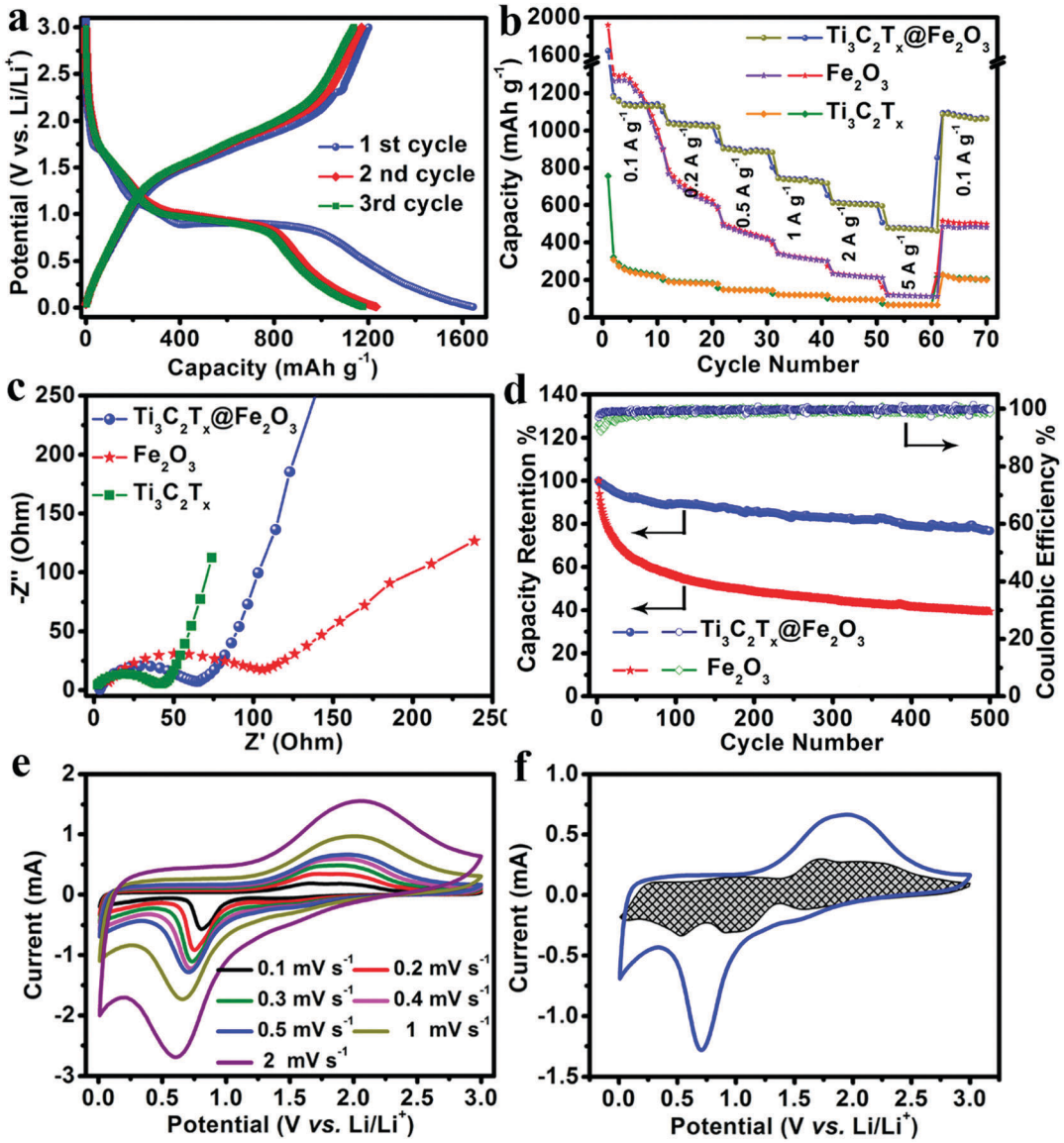

Fig. 3 Lithium storage performance of the Fe_2O_3, $Ti_3C_2T_x$ and $Ti_3C_2T_x$@Fe_2O_3 electrodes: (a) the first three charge–discharge cycles of the $Ti_3C_2T_x$@Fe_2O_3 hybrid electrode at a current density of 0.1 A g^{-1}. (b) Rate performances and (c) EIS of the Fe_2O_3, $Ti_3C_2T_x$ and $Ti_3C_2T_x$@Fe_2O_3 electrodes. (d) Cycling stability of the Fe_2O_3 and $Ti_3C_2T_x$@Fe_2O_3 electrodes at a current density of 5 A g^{-1}. (e) CV curves of a $Ti_3C_2T_x$@Fe_2O_3 electrode at different scan rates. (f) The capacity separation of the $Ti_3C_2T_x$@Fe_2O_3 hybrid electrode at a scan rate of 0.5 mV s^{-1}.

Impedance Spectroscopy (EIS) measurement (shown in Fig. 3c). The aerogel-like MXene anode exhibits a small charge transfer resistance (R_{ct}) of ~40 Ω, indicating its excellent conductivity. After loading Fe_2O_3 nanospheres on the conductive matrix, the $Ti_3C_2T_x$@Fe_2O_3 anode shows a reduced R_{ct} of ~60 Ω, which is noticeably lower than that of the purely Fe_2O_3 anode (~120 Ω). This proves that the conductive network can effectively increase the electroconductivity, thus leading to an enhanced rate performance. In addition, the long-term cycling stability of a hybrid anode has been observed as shown in Fig. 3d. The $Ti_3C_2T_x$@Fe_2O_3 anode demonstrates 0.042% fading rate per cycle at a current density of 5 A g^{-1} for up to 500 cycles, which is much lower than that of the bare Fe_2O_3 anode, and also lower than those of other previously reported Fe_2O_3-based anodes (such as hierarchical porous Fe_2O_3 nanosheets,[31] polypyrrole-coated Fe_2O_3@C composites[33] and 3D-graphene@Fe_2O_3,[28] *etc.*). In addition, Fig. S8 (ESI†) demonstrates the SEM images of the $Ti_3C_2T_x$@Fe_2O_3 electrode after cycling. It is noted that under the protection of the MXene, the Fe_2O_3 sphere still preserves the structure after the cycling. The above results convincingly confirm that the MXene matrix can effectively enhance the electrochemical performances of the $Ti_3C_2T_x$@Fe_2O_3 composite anodes.

In order to gain further insight into the electrochemistry of the electrode material, cyclic voltammetry (CV) measurements were performed. Fig. 3e depicts the CV curves of the $Ti_3C_2T_x$@Fe_2O_3 anode collected at different scan rates from 0.1 to 0.2, 0.3, 0.4, 0.5, 1 and 2 mV s^{-1}, which are well-consistent with the charge–discharge profiles. The charge storage behaviours of the $Ti_3C_2T_x$@Fe_2O_3 anode can be studied by separating the capacitive and diffusion-controlled currents *via* eqn (1).[42]

$$i(V) = k_1\nu + k_2\nu^{0.5} \quad (1)$$

where $i(V)$, $k_1\nu$, $k_2\nu^{0.5}$, and ν represent the current at a fixed voltage, the capacitive and diffusion controlled current and scan rate, respectively. Noticeably, 38% of the total capacity of the $Ti_3C_2T_x$@Fe_2O_3 anode comes from a capacitive process at the scan rate of 0.5 mV s^{-1} (Fig. 3f) while this value is boosted to 51% in the pristine aerogel-like $Ti_3C_2T_x$ MXene anode (Fig. S9, ESI†), indicating the change in storage behaviour after the introduction of an interconnected MXene matrix. In addition, the phase change of the nanocomposite during cyclic voltammetry measurement can be observed by *ex situ* XRD as shown in Fig. S10 (ESI†). The peak located at around 7° shifted to lower 2θ-angles during the cathodic scan, which indicates the intercalation of lithium ions into MXene layers. This confirms that the MXene matrix not only acts as a conductive network, but also does store some lithium ions, which delivers part of the capacity for the whole composite.

$Ti_3C_2T_x$@Fe_2O_3 anodes with improved rate and cycling performances have been achieved. Thus, development of matchable lithium-ion capacitor cathodes is highly desired to effectively enhance the electrochemical performances of full lithium-ion capacitors. In this regard, a 3-D nitrogen and sulphur dual-doped porous carbon (NS-DPC) derived from biomass has been synthesized as a cathode material to match $Ti_3C_2T_x$@Fe_2O_3 anodes. As presented in Fig. S11a (ESI†), the XRD pattern of the NS-DPC has no obvious peaks at 23° and 43.2°, which correspond to the (002) and (100) planes, respectively, indicating disordered carbon. The Raman spectrum of the NS-DPC is shown in Fig. S11b (ESI†), where the broad D band suggests a defect-induced structure while the G band indicates the graphitic layers and the tangential vibration of the carbon atoms. The ratio of I_D/I_G (I_D signifies the intensity of D band and I_G denotes the intensity of the G band) of the NS-DPC is determined to be 0.85, which indicates more structural distortion and defects in the as-prepared NS-DPC. Fig. S12a and b (ESI†) show the SEM images of the NS-DPC and it can be observed that the as-prepared material shows an interconnected porous architecture with pore sizes ranging from 500 nm to 1 μm. These are beneficial for the rapid diffusion of electrolyte during charge/discharge processes. The porous carbon was further characterized by TEM. Noticeably, large numbers of micro- and mesopores as well as channels have been detected in Fig. S13 (ESI†), suggesting a large surface area of porosity. The material shows a typical type II adsorption–desorption isotherm with a high nitrogen sorption capacity (Fig. S14a, ESI†).[55] The Brunauer–Emmett–Teller (BET) surface area and pore volume of NS-DPC is 1807 m^2 g^{-1} and 0.77 cm^3 g^{-1}, respectively. The pore size distribution (Fig. S14b, ESI†) is narrow with an average pore size less than 3 nm, again confirming the existence of mesopores. X-ray photoelectron spectra (XPS) were also taken to determine the elemental composition of the obtained NS-DPC (as displayed in Fig. S15, ESI†). The spectrum of N 1s (Fig. S15b, ESI†) can be deconvoluted into two peaks located at 400.2 and 402.2 eV, corresponding to graphitic nitrogen and pyridine nitrogen, respectively. Moreover, in Fig. S15c (ESI†), two fitted peaks can be assigned to carbon-bonded sulphur C–S–C (164.1 eV) and highly oxidized sulphur SO_x (167.9 eV), confirming the existence of an S element.[56]

The electrochemical performance of NS-DPC as the electrode for lithium-ion capacitors was tested in a two-electrode system with lithium foil as a counter and reference electrode and 1.0 M $LiPF_6$ (dissolved in EC/DEC, v/v = 1 : 1) as an electrolyte. As shown in Fig. 4a, CV measurements were carried out at scan rates from 5 mV s^{-1} to 50 mV s^{-1} with a potential window from 2.0 V to 4.5 V. The CV curves of the NS-DPC cathode maintain a good rectangular shape with scan rate increasing from 5 mV s^{-1} to 50 mV s^{-1}, suggesting an outstanding capacitive behaviour and rate performance. The small humps in the CV curves indicate the existence of a pseudocapacitive process, which can be ascribed to the interaction between the electrolyte and the nitrogen/sulphur atom defects. And this can also be confirmed by Fig. S16 (ESI†), in which 83% of the total capacity is assigned to the capacitive behaviour at a scan rate of 40 mV s^{-1}. Moreover, the CV curves still retain rectangular shapes without distortion as the potential window is increased from 3.5 to 4.5 V, confirming the stable capacitive behaviour of the NS-DPC cathode (Fig. 4b). Linear charge–discharge curves at different current densities from 0.1 A g^{-1} to 10 A g^{-1} can be observed for the NS-DPC cathode in Fig. S17 (ESI†), suggesting rapid capacitive behaviour. Fig. 4c presents the rate performance of an NS-DPC cathode, exhibiting ~140 mA h g^{-1} at a current density of 0.1 A g^{-1}. This value is much higher than that of porous carbon without any doping

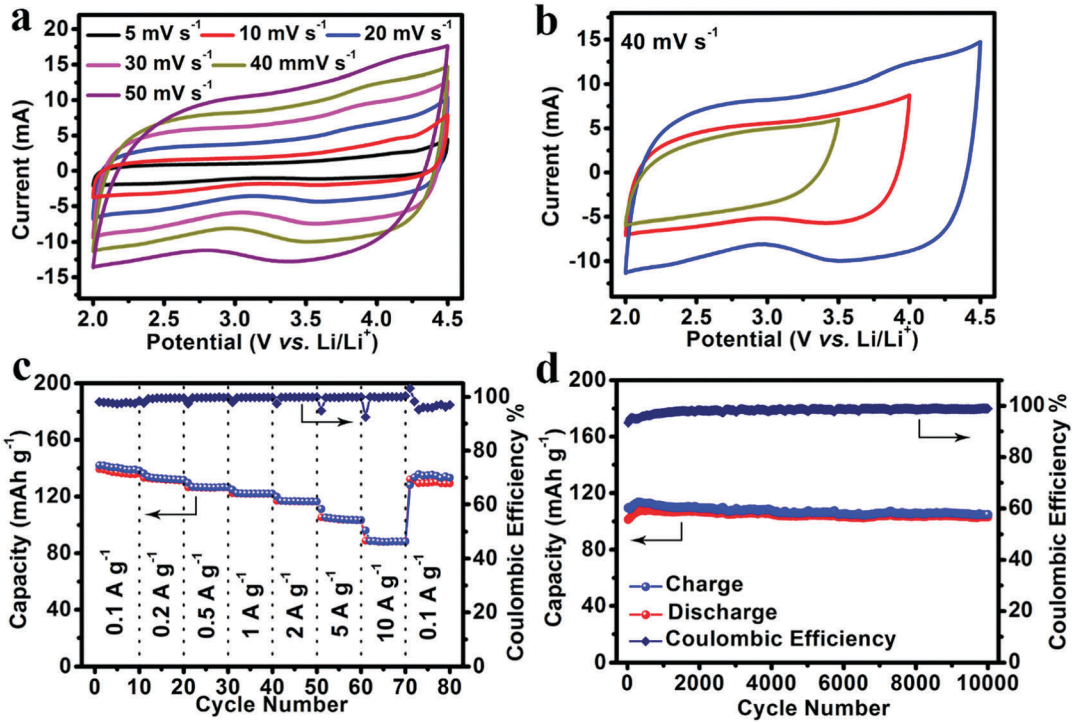

Fig. 4 Lithium storage performance of the NS-DPC cathode tested in a $LiPF_6$ electrolyte: (a) CV curves of the NS-DPC cathode at different scan rates. (b) CV curves of the NS-DPC cathode cycled within different potential windows at 40 mV s^{-1}. (c) Rate performance of a NS-DPC cathode. (d) Cycling stability of a NS-DPC cathode at a current density of 5 A g^{-1}.

(shown in Fig. S18, ESI†), also higher than those of previously reported activated carbon materials in a similar potential window.[10] Furthermore, a specific capacity of ~91 mA h g^{-1} was achieved even at a high current density of 10 A g^{-1}, corresponding to ~64% capacity retention with the current density increasing from 0.1 A g^{-1} to 10 A g^{-1}, which confirms the superior rate capability of the NS-DPC cathodes. Except for excellent rate capability, the NS-DPC cathode material also possesses an outstanding cycling stability, showing a slight increase of ~3% of the initial capacity for the NS-DPC cathode after 10 000 cycles. This may be attributed to the activation of the NS-DPC cathode material, explicitly confirming the great cycling performance of the NS-DPC cathode. It is noted that the excellent capacitive performance can be attributed to the natural features of the biomass, including heteroatoms and natural templates.

As an effective method to boost both the energy density and power density, we constructed lithium-ion full capacitors based on the as-prepared NS-DPC cathode and the prelithiated $Ti_3C_2T_x$@Fe_2O_3 anode (Fig. S19, ESI†). The LIC device with 4 V potential window was fabricated by using a 1 M $LiPF_6$ electrolyte. As schematically depicted in Fig. 5a, since LICs combine the characteristics of both LIBs and SCs by utilizing the LIB anode and SC cathode, Li^+ ions will intercalate into MXene layers and react with Fe_2O_3 hollow nanospheres, while the PF_6^- in the electrolyte is absorbed onto the surface of the NS-DPC cathode during the charge process. The discharge process is the reverse of the charge process. Compared with conventional SCs, LICs have an asymmetric configuration, thus improving the energy density because of the intake of a high-capacity anode with its faradaic based storage mechanism. Meanwhile, unlike LIBs, LICs consume both cations and anions, which can provide faster kinetics than the rocking chair type reaction in LIBs.[5,10,57,58] Fig. 5b demonstrates the cyclic voltammetry curves of the $Ti_3C_2T_x$@Fe_2O_3//NS-DPC LIC device at scan rates ranging from 5–50 mV s^{-1} in a voltage window between 0.01 and 4 V. The CV curves display a quasi-rectangular shape even at a high scan rate of 50 mV s^{-1}, suggesting superior capacitive behaviour and fast charge–discharge capability of the as-assembled full lithium-ion capacitor. Furthermore, the prolonged and symmetric charge–discharge curves at different current densities exhibit a near-linear slope with a slight internal resistance (IR) drop (Fig. 5c), again confirming the good capacitive behaviour of the device. A high specific capacity of 109 mA h g^{-1} (based on the total mass of cathodic and anodic active materials) is achieved at a current density of 0.2 A g^{-1}, which is much higher than other previously reported values for LICs.[10,29,59]

Energy density and power density are two important parameters for evaluation of the as-assembled $Ti_3C_2T_x$@Fe_2O_3// NS-DPC LIC device. Thus, the comparisons of energy density and power density of the $Ti_3C_2T_x$@Fe_2O_3//NS-DPC LIC device and other previously reported results are summarized in a Ragone plot (shown in Fig. 5d).[60–67] It can be seen that the $Ti_3C_2T_x$@Fe_2O_3//NS-DPC LIC device delivers a high energy density of 216 W h kg^{-1} at a power density of 400 W kg^{-1}. Even at a high power density of 20 kW kg^{-1}, the device can still

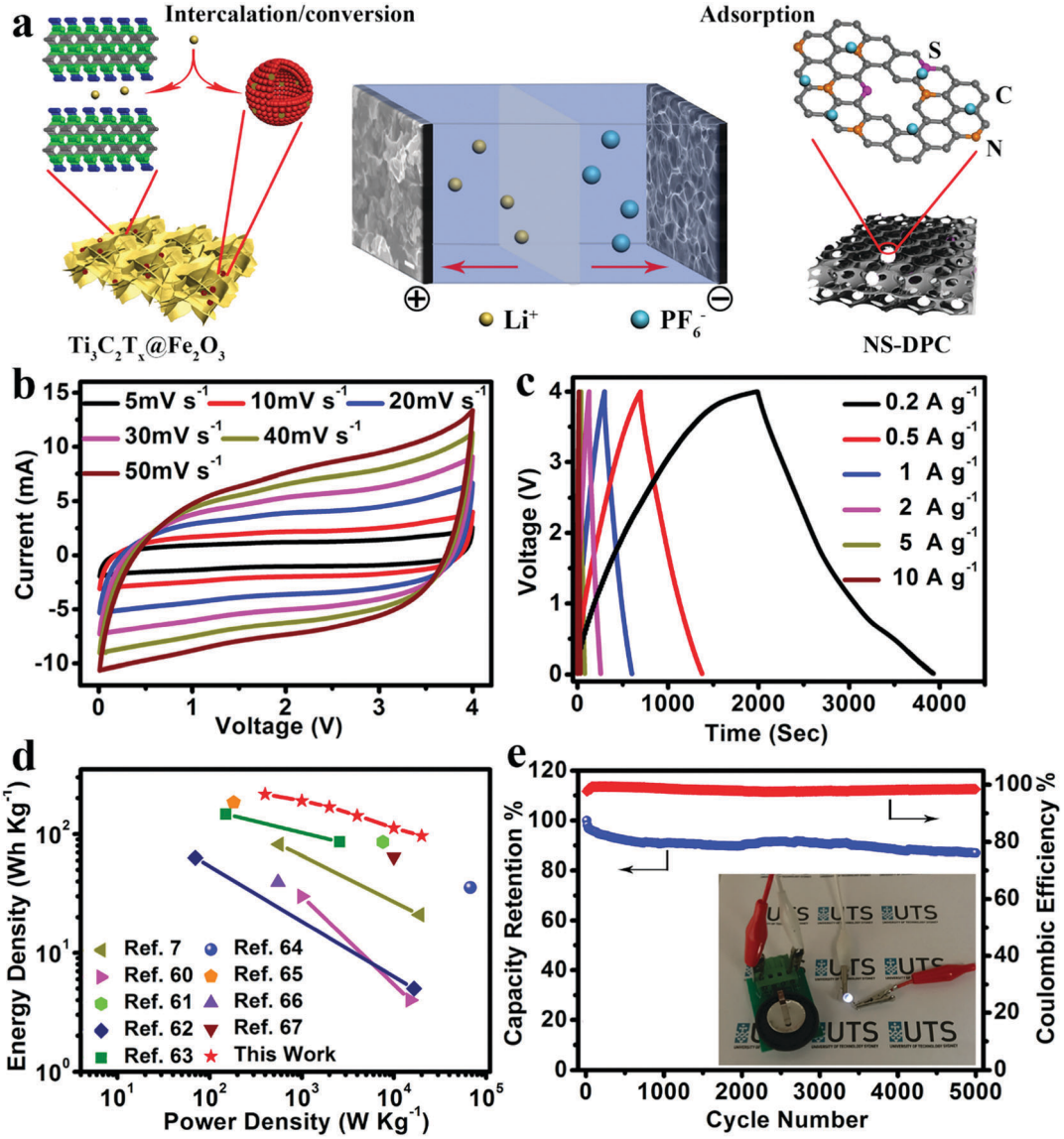

Fig. 5 (a) Schematic illustration of the charge-storage mechanisms for the $Ti_3C_2T_x$@Fe_2O_3//NS-DPC LIC device. (b) CV curves and (c) charge–discharge curves of the $Ti_3C_2T_x$@Fe_2O_3//NS-DPC LIC device. (d) Ragone plots of the $Ti_3C_2T_x$@Fe_2O_3//NS-DPC LIC device and other previously reported devices. (e) Cycling stability of the $Ti_3C_2T_x$@Fe_2O_3//NS-DPC device at a current density of 5 A g^{-1}; the inset is a demonstration of the LIC device powering an LED.

achieve 96.5 W h kg^{-1}, which is superior to the previously reported lithium-ion capacitors (see details in Tables S1 and S2 in ESI†). Those include $Li_4Ti_5O_{12}$/graphene//AC (4 W h kg^{-1} at 15 kW kg^{-1}),[60] TiO_2//graphene (21 W h kg^{-1} at 19 kW kg^{-1}),[7] hard carbon//AC (85.7 W h kg^{-1} at 7.6 kW kg^{-1})[61] and Nb_2O_5/C//AC (5 W h kg^{-1} at 16.5 kW kg^{-1}),[62] *etc.* Except for the high energy and power density of the as-assembled device, it also exhibits outstanding cycling stability, retaining 87% of the initial capacity at 5 A g^{-1} after 5000 cycles, as shown in Fig. 5e. In addition, the as-assembled $Ti_3C_2T_x$@Fe_2O_3// NS-DPC LIC device is able to power a 2.5 V light-emitting diode (LED), suggesting that the $Ti_3C_2T_x$@Fe_2O_3//NS-DPC LIC device possesses promising expectations for practical applications (see inset of Fig. 5e).

Conclusions

In summary, for the first time, we successfully designed and synthesized an interconnected aerogel-like MXene wrapped Fe_2O_3 nanosphere nanocomposite as an anode material for lithium-ion capacitors. The $Ti_3C_2T_x$ MXene as a highly conductive matrix affords fast transport of electrons, while the Fe_2O_3 hollow nanospheres provide large specific capacity, thus synergizing to enhance the electrochemical performance of composite electrodes. Consequently, owing to the nanostructural pillar effect and combined synergistic effects, the $Ti_3C_2T_x$@Fe_2O_3 nanocomposite delivers a high reversible capacity of 1180 mA h g^{-1} at a current density of 0.1 A g^{-1} with excellent rate performance and cycling stability. A 4 V lithium-ion capacitor has been assembled

based on the MXene wrapped Fe_2O_3 nanosphere anode and the 3D nitrogen sulphur dual-doped porous carbon cathode, showing a maximum capacity of 109 mA h g^{-1}. The highest energy density of 216 W h kg^{-1} at a power density of 400 W kg^{-1} and the highest power density of 20 kW kg^{-1} at an energy density of 96.5 W h kg^{-1} have been achieved by $Ti_3C_2T_x$@Fe_2O_3//NS-DPC LIC devices, confirming both high energy density and power density of the fabricated lithium-ion capacitor. These features together endow the $Ti_3C_2T_x$@Fe_2O_3//NS-DPC LIC device with promising energy storage density for practical devices and applications.

Conflicts of interest

There are no conflicts to declare.

Acknowledgements

This work was financially supported by the Australian Renewable Energy Agency (ARENA) project (ARENA 2014/RND106) and the Australian Research Council (ARC) through the ARC Discovery Project (DP170100436). X. T. acknowledges the financial support from the China scholarship council (CSC grant number: 201606840117). The authors thank Prof. Yury Gogotsi (Department of Materials Science and Engineering and A. J. Drexel Nanomaterials Institute, Drexel University, Philadelphia, PA19104, USA) for providing MAX phase Ti_3AlC_2 materials.

References

1 M. Armand and J. M. Tarascon, *Nature*, 2008, **451**, 652–657.
2 D. Dubal, O. Ayyad, V. Ruiz and P. Gomez-Romero, *Chem. Soc. Rev.*, 2015, **44**, 1777–1790.
3 K. Yuan, T. Hu, Y. Xu, R. Graf, L. Shi, M. Forster, T. Pichler, T. Riedl, Y. Chen and U. Scherf, *Mater. Chem. Front.*, 2017, **1**, 278–285.
4 M. Cheng, Y. Meng, Q. Meng, L. Mao, M. Zhang, K. Amin, A. Ahmad, S. Wu and Z. Wei, *Mater. Chem. Front.*, 2018, **2**, 986–992.
5 H. Wang, C. Zhu, D. Chao, Q. Yan and H. J. Fan, *Adv. Mater.*, 2017, **29**, 1702093.
6 G. G. Amatucci, F. Badway, A. Du Pasquier and T. Zheng, *J. Electrochem. Soc.*, 2001, **148**, A930–A939.
7 H. Wang, C. Guan, X. Wang and H. J. Fan, *Small*, 2015, **11**, 1470–1477.
8 F. Zhang, T. Zhang, X. Yang, L. Zhang, K. Leng, Y. Huang and Y. Chen, *Energy Environ. Sci.*, 2013, **6**, 1623–1632.
9 Y. Ma, H. Chang, M. Zhang and Y. Chen, *Adv. Mater.*, 2015, **27**, 5296–5308.
10 Q. Xia, H. Yang, M. Wang, M. Yang, Q. Guo, L. Wan, H. Xia and Y. Yu, *Adv. Energy Mater.*, 2017, **7**, 1701336.
11 Q. Wang, Z. Wen and J. Li, *Adv. Funct. Mater.*, 2006, **16**, 2141–2146.
12 L. Gao, D. Huang, Y. Shen and M. Wang, *J. Mater. Chem. A*, 2015, **3**, 23570–23576.
13 H. Kim, M. Y. Cho, M. H. Kim, K. Y. Park, H. Gwon, Y. Lee, K. C. Roh and K. Kang, *Adv. Energy Mater.*, 2013, **3**, 1500–1506.
14 E. Lim, H. Kim, C. Jo, J. Chun, K. Ku, S. Kim, H. I. Lee, I. S. Nam, S. Yoon and K. Kang, *ACS Nano*, 2014, **8**, 8968–8978.
15 L. Cheng, H. Q. Li and Y. Y. Xia, *J. Solid State Electrochem.*, 2016, **10**, 405–410.
16 A. Banerjee, K. K. Upadhyay, D. Puthusseri, V. Aravindan, S. Madhavi and S. Ogale, *Nanoscale*, 2014, **6**, 4387–4394.
17 V. Aravindan, D. Mhamane, W. C. Ling, S. Ogale and S. Madhavi, *ChemSusChem*, 2013, **6**, 2240–2244.
18 K. Leng, F. Zhang, L. Zhang, T. Zhang, Y. Wu, Y. Lu, Y. Huang and Y. Chen, *Nano Res.*, 2013, **6**, 581–592.
19 T. Aida, K. Yamada and M. Morita, *Electrochem. Solid-State Lett.*, 2006, **9**, A534–A536.
20 S. Sivakkumar and A. Pandolfo, *Electrochim. Acta*, 2012, **65**, 280–287.
21 V. Khomenko, E. Raymundo-Piñero and F. Béguin, *J. Power Sources*, 2008, **177**, 643–651.
22 J. H. Kim, J. S. Kim, Y. G. Lim, J. G. Lee and Y. J. Kim, *J. Power Sources*, 2011, **196**, 10490–10495.
23 K. Karthikeyan, S. Amaresh, S. N. Lee, V. Aravindan and Y. S. Lee, *Chem. – Asian J.*, 2014, **9**, 852–857.
24 J. H. Won, H. M. Jeong and J. K. Kang, *Adv. Energy Mater.*, 2017, **7**, 1601355.
25 X. Liu, H. G. Jung, S. O. Kim, H. S. Choi, S. Lee, J. H. Moon and J. K. Lee, *Sci. Rep.*, 2013, **3**, 3183.
26 P. Yang, Y. Ding, Z. Lin, Z. Chen, Y. Li, P. Qiang, M. Ebrahimi, W. Mai, C. P. Wong and Z. L. Wang, *Nano Lett.*, 2014, **14**, 731–736.
27 X. Tang, R. Jia, T. Zhai and H. Xia, *ACS Appl. Mater. Interfaces*, 2015, **7**, 27518–27525.
28 T. Jiang, F. Bu, X. Feng, I. Shakir, G. Hao and Y. Xu, *ACS Nano*, 2017, **11**, 5140–5147.
29 J. Wang, H. Tang, H. Wang, R. Yu and D. Wang, *Mater. Chem. Front.*, 2017, **1**, 414–430.
30 J. M. Jeong, B. G. Choi, S. C. Lee, K. G. Lee, S. J. Chang, Y. K. Han, Y. B. Lee, H. U. Lee, S. Kwon and G. Lee, *Adv. Mater.*, 2013, **25**, 6250–6255.
31 K. Cao, L. Jiao, H. Liu, Y. Liu, Y. Wang, Z. Guo and H. Yuan, *Adv. Energy Mater.*, 2015, **5**, 1401421.
32 Z. Ma, X. Huang, S. Dou, J. Wu and S. Wang, *J. Phys. Chem. C*, 2014, **118**, 17231–17239.
33 F. Han, D. Li, W. C. Li, C. Lei, Q. Sun and A. H. Lu, *Adv. Funct. Mater.*, 2013, **23**, 1692–1700.
34 N. Zhang, X. Han, Y. Liu, X. Hu, Q. Zhao and J. Chen, *Adv. Energy Mater.*, 2015, **5**, 1401123.
35 G. Gao, L. Yu and H. B. Wu, *Small*, 2014, **10**, 1741–1745.
36 Y. Zeng, Y. Han, Y. Zhao, Y. Zeng, M. Yu, Y. Liu, H. Tang, Y. Tong and X. Lu, *Adv. Energy Mater.*, 2015, **5**, 1402176.
37 B. Ahmed, D. H. Anjum, Y. Gogotsi and H. N. Alshareef, *Nano Energy*, 2017, **34**, 249–256.
38 X. Wang, S. Kajiyama, H. Iinuma, E. Hosono, S. Oro, I. Moriguchi, M. Okubo and A. Yamada, *Nat. Commun.*, 2015, **6**, 6544.
39 J. Luo, X. Tao, J. Zhang, Y. Xia, H. Huang, L. Zhang, Y. Gan, C. Liang and W. Zhang, *ACS Nano*, 2016, **10**, 2491–2499.

40 M. Ghidiu, M. R. Lukatskaya, M. Q. Zhao, Y. Gogotsi and M. W. Barsoum, *Nature*, 2014, **516**, 78–81.
41 L. Li, Y. Chu, Y. Liu and L. Dong, *J. Phys. Chem. C*, 2007, **111**, 2123–2127.
42 X. Xie, M. Q. Zhao, B. Anasori, K. Maleski, C. E. Ren, J. Li, B. W. Byles, E. Pomerantseva, G. Wang and Y. Gogotsi, *Nano Energy*, 2016, **26**, 513–523.
43 M. Q. Zhao, C. E. Ren, Z. Ling, M. R. Lukatskaya, C. Zhang, K. L. Van Aken, M. W. Barsoum and Y. Gogotsi, *Adv. Mater.*, 2015, **27**, 339–345.
44 J. Yan, C. E. Ren, K. Maleski, C. B. Hatter, B. Anasori, P. Urbankowski, A. Sarycheva and Y. Gogotsi, *Adv. Funct. Mater.*, 2017, **27**, 1701264.
45 M. R. Lukatskaya, O. Mashtalir, C. E. Ren, Y. Dall Agnese, P. Rozier, P. L. Taberna, M. Naguib, P. Simon, M. W. Barsoum and Y. Gogotsi, *Science*, 2013, **341**, 1502–1505.
46 M. Q. Zhao, X. Xie, C. E. Ren, T. Makaryan, B. Anasori, G. Wang and Y. Gogotsi, *Adv. Mater.*, 2017, **29**, 1702410.
47 Y. Ma, B. Li and S. Yang, *Mater. Chem. Front.*, 2018, **2**, 456–467.
48 D. De Faria, S. Venâncio Silva and M. De Oliveira, *J. Raman Spectrosc.*, 1997, **28**, 873–878.
49 M. Hu, Z. Li, T. Hu, S. Zhu, C. Zhang and X. Wang, *ACS Nano*, 2016, **10**, 11344–11350.
50 T. Fujii, F. De Groot, G. Sawatzky, F. Voogt, T. Hibma and K. Okada, *Phys. Rev. B: Condens. Matter Mater. Phys.*, 1999, **59**, 3195.
51 S. Xu, C. M. Hessel, H. Ren, R. Yu, Q. Jin, M. Yang, H. Zhao and D. Wang, *Energy Environ. Sci.*, 2014, **7**, 632–637.
52 X. Liang, A. Garsuch and L. F. Nazar, *Angew. Chem., Int. Ed.*, 2015, **54**, 3907–3911.
53 B. Ahmed, D. H. Anjum, M. N. Hedhili, Y. Gogotsi and H. N. Alshareef, *Nanoscale*, 2016, **8**, 7580–7587.
54 X. Liang, Y. Rangom, C. Y. Kwok, Q. Pang and L. F. Nazar, *Adv. Mater.*, 2017, **29**, 1603040.
55 J. Deng, T. Xiong, F. Xu, M. Li, C. Han, Y. Gong, H. Wang and Y. Wang, *Green Chem.*, 2015, **17**, 4053–4060.
56 Q. Pang, J. Tang, H. Huang, X. Liang, C. Hart, K. C. Tam and L. F. Nazar, *Adv. Mater.*, 2015, **27**, 6021–6028.
57 D. Xu, D. Chao, H. Wang, Y. Gong, R. Wang, B. He, X. Hu and H. J. Fan, *Adv. Energy Mater.*, 2018, **8**, 1702769.
58 H. Wang, G. Jia, Y. Guo, Y. Zhang, H. Geng, J. Xu, W. Mai, Q. Yan and H. J. Fan, *Adv. Mater. Interfaces*, 2016, **3**, 1600375.
59 M. Yang, Y. Zhong, J. Ren, X. Zhou, J. Wei and Z. Zhou, *Adv. Energy Mater.*, 2015, **5**, 1500550.
60 N. Xu, X. Sun, X. Zhang, K. Wang and Y. Ma, *RSC Adv.*, 2015, **5**, 94361–94368.
61 J. Zhang, X. Liu, J. Wang, J. Shi and Z. Shi, *Electrochim. Acta*, 2016, **187**, 134–142.
62 E. Lim, C. Jo, H. Kim, M. H. Kim, Y. Mun, J. Chun, Y. Ye, J. Hwang, K. S. Ha and K. C. Roh, *ACS Nano*, 2015, **9**, 7497–7505.
63 F. Zhang, T. F. Zhang, X. Yang, L. Zhang, K. Leng, Y. Huang and Y. S. Chen, *Energy Environ. Sci.*, 2013, **6**, 1623–1632.
64 H. W. Wang, Y. Zhang, H. X. Ang, Y. Q. Zhang, H. T. Tan, Y. F. Zhang, Y. Y. Guo, J. B. Franklin, X. L. Wu, M. Srinivasan, H. J. Fan and Q. Y. Yan, *Adv. Funct. Mater.*, 2016, **26**, 3082–3093.
65 H. L. Wang, Z. W. Xu, Z. Li, K. Cui, J. Ding, A. Kohandehghan, X. Tan, B. Zahiri, B. C. Olsen, C. M. Holt and D. Mitlin, *Nano Lett.*, 2014, **14**, 1987–1994.
66 R. Ding, L. Qi and H. Y. Wang, *RSC Adv.*, 2013, **3**, 12581–12584.
67 R. T. Wang, J. W. Lang, P. Zhang, Z. Y. Lin and X. B. Yan, *Adv. Funct. Mater.*, 2015, **25**, 2270–2278.